X-ray diffuse scattering study of vacancy nanoclusters in homoepitaxial Ag(001) films

Chinkyo Kim
Department of Physics and Research Institute for Basic Sciences, Kyung Hee University, 26 Kyunghee-daero, Dongdaemun-gu, Seoul 130-701, Korea

Edward H. Conrad
School of Physics, Georgia Institute of Technology, Atlanta, Georgia 30332, USA

Paul F. Miceli*
Department of Physics and Astronomy, University of Missouri at Columbia, Columbia, Missouri 65211, USA
(Received 21 May 2012; revised manuscript received 3 September 2012; published 24 October 2012)

The analysis of x-ray diffuse scattering measurements on Ag homoepitaxial films is presented. The experiments, which establish that a low concentration of large vacancy clusters can be incorporated into noble metals during homoepitaxial growth, were performed on 100 monolayer films of Ag deposited on Ag(001) at low temperature. The diffuse scattering of this film was measured, *in situ*, near several in-plane Bragg positions in grazing-incidence geometry. Because of the large dilatation from the vacancy clusters, the usual approximations of Huang and Stokes-Wilson scattering cannot be made and it is shown that numerical integration of the diffuse scattering equations leads to good agreement between the data and a point-defect scattering model.

DOI: 10.1103/PhysRevB.86.155446 PACS number(s): 68.35.Dv, 61.05.cf, 81.15.Hi

I. INTRODUCTION

As technology and science move towards ever decreasing length scales, there is considerable motivation to understand the physical principles that control the growth and evolution of nanoscale materials. Consequently, there has been extensive experimental as well as theoretical investigation of growth processes, particularly for noble metal homoepitaxy whose simplicity can help reveal the essential atomic-scale mechanisms.[1] Simulations of growth at surfaces on sufficiently large systems are typically performed using kinetic Monte Carlo (KMC) methods, which require input knowledge about the basic kinetic steps that dictate the growth of films that are far from equilibrium. Each kinetic mechanism, such as nucleation, the diffusion on terraces, and the hopping both across and along step edges, must be specifically included. Such simulations also require knowledge of the corresponding kinetic barriers, which is best obtained through comparisons to experiments.

What has not been widely explored during epitaxial crystal growth, however, is the subsurface region. Generally, the ideal crystalline atomic positions have been assumed. For example, in KMC simulations, atoms that deposit at crystalline step edges are "funneled"[2] into crystalline sites in order to preserve the crystal geometry and to *explicitly eliminate* the formation of vacancies.[3] Similarly, on the experimental side, scanning-probe techniques that are typically used to study the growth behavior at surfaces cannot see below the surface. Therefore, there has been little impetus to consider the incorporation of subsurface defects. Nevertheless, x-ray reflectivity experiments on the low-temperature homoepitaxial growth of several noble-metal surfaces have shown a large amount of compressive strain, on the order of 1%.[4–6] This strain, which can be annealed out at the known annealing temperature for vacancies in these metals, was attributed to the incorporation of vacancies during epitaxial growth, although the experiments could not distinguish between monovacancies and vacancy clusters.[5] In addition, Botez *et al.*[5] found that the strain increased with decreasing temperature concomitantly with a low-temperature reentrant roughening observed by STM[7,8]. The reentrant roughening was reproduced in KMC simulations by relaxing the funneling condition which introduced internal voids or vacancy clusters, thereby giving theoretical support for the presence of such incorporated defects.[9]

An alternative explanation was later suggested by Shim *et al.*[10] whose accelerated molecular dynamics (MD) simulations reported that *large* off-normal deposition angles cause nanoscale surface roughness which, in turn, leads to compressive strain comparable in size to that observed in the x-ray reflectivity studies. However, x-ray diffuse scattering experiments by Kim *et al.*, performed for 100 monolayer (ML) Ag(001) homoepitaxial films grown at a considerably *smaller* off-normal deposition angle, revealed point-defect scattering that provides clear experimental evidence for the existence of large vacancy clusters.[11] Although nanoroughness-induced strain is plausible,[12] the diffuse scattering experiments establish the presence of vacancy clusters in relatively thicker films (100 ML) where surface-induced contributions to strain would be small. It should also be noted that the concentration of the vacancy clusters in the experiments was found to be extremely low, and therefore more difficult to observe in MD simulations, although each cluster contributes a large displacement field.

In practice, there are few experimental tools to directly probe the vacancies themselves within a thin film.[13,14] The alternative approach is to measure the displacement field arising from the vacancies. X-ray diffuse scattering measured near a Bragg peak is very sensitive to the static displacement of the atoms from their ideal crystalline positions and, by maintaining the incident and scattered beams near grazing angles with respect to the surface, one can have a greater sensitivity to the atomic displacements near the surface as compared to positions deeper in the sample. It is important to recognize that diffuse scattering measurements differ significantly from the earlier reflectivity measurements: the latter measures the average (*long-range*) strain whereas the former measures the (*local*) elastic distortion around a defect.

Thus, the diffuse scattering is directly tied to localized defects. Moreover, the theoretical model to calculate the diffuse scattering intensity is well developed so that the structural characterization of vacancies can be done in a quantitative manner.[15] X-ray diffuse scattering has been extensively used to study point defects in metals and semiconductors[16,17] where the diffuse scattering intensity calculations typically employ the approximation that the displacement field is small, so that the intensity can be expanded in a power series in $1/q$. Here, $\mathbf{q} \equiv \mathbf{Q} - \mathbf{Q}_n$, where $\mathbf{Q}$ is the wave-vector transfer and $\mathbf{Q}_n$ is the reciprocal-lattice vector of the nearest Bragg peak. This approximation significantly simplifies the intensity calculation and, depending on the regime in which the diffuse scattering is measured, it results in the diffuse intensity varying as $1/q^2$ (Huang scattering, measured close to the Bragg peak) or $1/q^4$ (Stokes-Wilson scattering, measured farther from the Bragg peak). However, these approximations are not valid if the displacement field is too large. A crucial and central point of the present work is that the analysis of diffuse scattering from large vacancy clusters is complicated by the fact that their displacement fields are very large, which requires a different strategy for treating these systems.

In this paper, we present a detailed account of the diffuse x-ray scattering measurements and analysis by Kim *et al.*[11] The main conclusion is that the data are well described by a point defect scattering model having a large negative displacement volume due to vacancy clusters. It is shown that one cannot make the conventional approximations that lead to the Huang and Stokes-Wilson scattering regimes because the displacement field due to the vacancy clusters is very large. However, by numerically calculating the full diffuse scattering model for point defects, without making the conventional approximations, it is shown that excellent agreement between the measurements and the point-defect scattering model is achieved. More importantly, the ability to accurately describe these data by the full point-defect model gives clear evidence of large vacancy clusters forming in low-temperature homoepitaxially grown Ag films.

II. EXPERIMENT

The experiments were performed at the Advanced Photon Source Sector 6 beamline at Argonne National Laboratory. The surface preparation, film growth, and x-ray scattering measurements were carried out in an ultrahigh vacuum growth and analysis chamber that is integrated with a ψ diffractometer which is resident at the beamline. The base pressure of the chamber was 10^{-10} Torr and the clean surface was prepared by cycles of Ar ion sputtering and high-temperature thermal annealing. After a few iterations of this surface cleaning procedure, Auger electron spectroscopy (AES) measurements confirmed that there was no trace of contaminants on the clean surface within its sensitivity.

Homoepitaxial films of Ag, 100 monolayers (MLs) in thickness, were prepared by thermal evaporation of 99.9999% pure Ag from a pyrolytic boron nitride crucible onto the Ag(001) substrate, which was maintained at 150 K during the deposition as well as during all of the x-ray scattering measurements. The evaporation rate was 3.2 monolayers per minute, which was determined from the period of intensity oscillation that was measured during Ag deposition at the (001) anti-Bragg position. The angle at which Ag was deposited onto the substrate was 30° relative to the sample normal, as was dictated by the geometry of the surface chamber. The experiments could be repeated by annealing at 700 °C in order to regain the starting substrate.

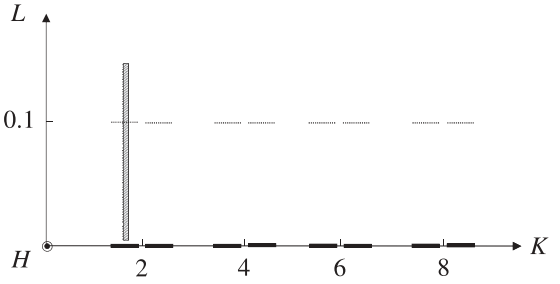

FIG. 1. Schematic diagram in reciprocal space showing the measurement and calculation details. Experimental measurements were carried out along the [0, K, 0.1] direction as shown by the thin horizontal lines. The shaded rectangular region schematically shows the resolution function of the detector at one measurement point, indicating that the intensity is integrated along the surface normal, from $L = 0.005$ to $L = 0.15$. The thick solid lines on the K axis show where the numerical calculation of diffuse scattering intensity was performed. Note that the scale is exaggerated in the diagram: it is highly elongated along L and compressed along K.

The diffuse scattering intensity was first measured for the clean Ag(001) surface and then subsequently measured for a surface on which a Ag film had been deposited. This allowed for the subtraction of the diffuse scattering that was intrinsic to the bulk crystal. The measurements were carried out in grazing incidence geometry in the vicinity of four Bragg reflections (H,K,L), indexed in reciprocal-lattice units of Ag, with $L = 0.1$, where L is taken to be along the surface normal. Scans were performed along the K direction near the Bragg positions at $K_n = 2, 4, 6, 8$ with $H = 0$. Figure 1 schematically shows where the diffuse scattering was measured in reciprocal space. The shaded rectangle indicates the resolution function of the detector at one data point. Since we fully opened the horizontal detector slit, the diffuse intensity was integrated along the surface normal direction from $L = 0.005$ to $L = 0.15$. The vertical slit size was set in such a way that the resolution was narrow enough so that there was no overlap among the data points along the K direction. The thick solid lines represent where the numerical calculation of the diffuse scattering intensity was carried out, which will be discussed later in detail.

III. RESULTS AND DISCUSSION

Figure 2 shows the x-ray diffuse scattering data obtained in the vicinity of the four Bragg peaks *before* and *after* the deposition of 100 MLs of Ag. Among the many sources of diffuse scattering, we are only interested in the diffuse scattering due to the defects in the 100-ML film. The only way to accomplish this is to subtract the diffuse scattering obtained before deposition from the *total* diffuse scattering measured after deposition. In this manner, extraneous contributions to the diffuse scattering from the Ag substrate, including thermal diffuse scattering, are removed. It should also be noted that

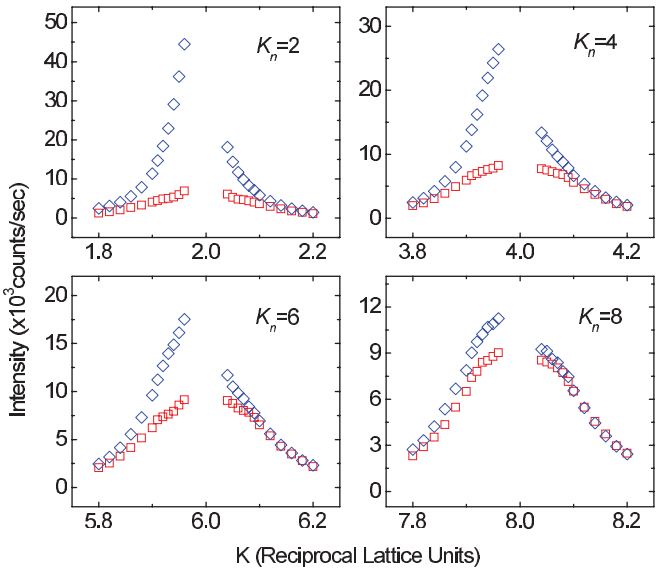

FIG. 2. (Color online) Diffuse x-ray scattering data for Ag/Ag(001) obtained along [0, K, 0.1] in the vicinity of four Bragg positions, K_n. It was measured for the clean starting surface (squares) and with 100 MLs of deposited Ag (diamonds).

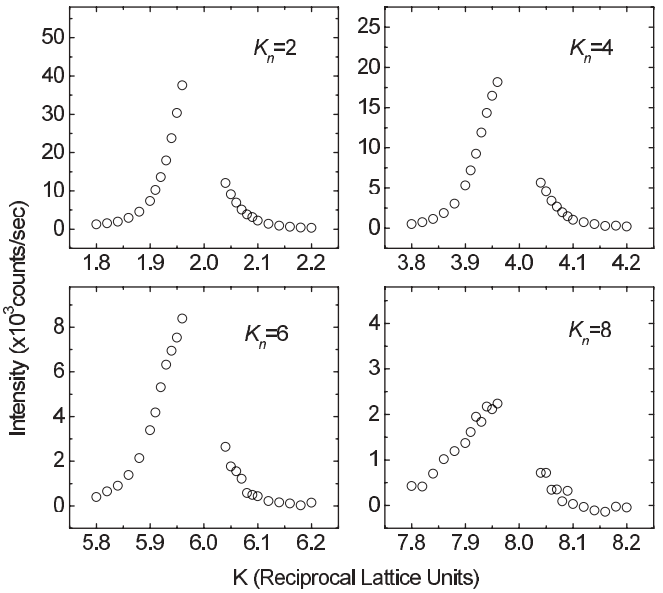

FIG. 3. The x-ray diffuse scattering intensity is shown for the 100-ML Ag(001) film. It was obtained by subtracting the diffuse scattering measured on the clean starting substrate from the total scattering measured on the substrate containing the deposited film. Note that the distribution of diffuse scattering around the Bragg positions is asymmetric toward lower K and that the intensity decreases rapidly with increasing K_n.

diffuse scattering due to surface roughening, which results from film deposition, will be zero at the Bragg peak and it will increase only as one moves away from the Bragg position along the surface normal direction, L. Since our measurements of the diffuse scattering were taken near the Bragg peaks for very small values of L, our measurements are not sensitive to the surface roughening; but they are sensitive to the static displacement of atoms within the film due to localized defects. In what follows, the diffuse scattering intensity will always refer to the *subtracted* diffuse scattering, which is shown in Fig. 3.

In general, it is known that point defects introduce an asymmetry to the diffuse scattering about the Bragg position:[18] the intensity is higher on the low-K side for vacancy defects whereas it is higher on the high-K side for interstitials. Figure 3 clearly reveals that the diffuse scattering has higher intensity on the lower-K side for each of the four Bragg positions, indicating that the origin of the diffuse scattering is from vacancies rather than from interstitials. It is also observed that the diffuse scattering intensity decreases rapidly in going from lower- to higher-order Bragg positions, K_n, which suggests that there is a high degree of static disorder.

For a quantitative analysis, we need to consider a theoretical model for the diffuse scattering that not only contains the point defects, but also includes the modification of the scattering that arises from the influence of the interfaces of a thin film on the elastic fields. Although a completely general model is not available, we can get some guidance from Barabash and Krivoglaz[15,19] who have calculated the diffuse scattering in the limit of small displacements from point defects in a homoepitaxial film; their result is given by

$$I(\mathbf{Q}) = N_d\, e^{-2M} |F|^2 (a^{\mathrm{o}})^2 \left(\frac{(\mathbf{Q}\cdot\mathbf{q})^2}{q^4} - 2\frac{\mathbf{Q}\cdot\mathbf{q}}{q^2} \frac{\mathrm{Re}[c_L(q_{||}+iq_z)\Phi]}{d} + \frac{c_L(2q_{||})|\Phi|^2}{d} \right),$$

$$\Phi \equiv \frac{1}{2}\left(\frac{1}{q_{||}+iq_z} - \frac{3-4\sigma}{q_{||}-iq_z} \right)\left(\frac{\mathbf{Q}_{||}\cdot\mathbf{q}_{||}}{q_{||}} + iQ_z \right) + \frac{q_{||}}{(q_{||}-iq_z)^2}\left(\frac{\mathbf{Q}_{||}\cdot\mathbf{q}_{||}}{q_{||}} - iQ_z \right), \quad (1)$$

$$M \equiv c\sum_{s'}[1-\cos(\mathbf{Q}\cdot\mathbf{u}_{ss'})], \quad c_L(p) \equiv \frac{d}{D_e}\int_0^{D_e} e^{-pz}dz,$$

$$\mathbf{q} \equiv \mathbf{Q} - \mathbf{Q}_n, \quad a^{\mathrm{o}} \equiv \frac{1+\sigma}{3(1-\sigma)}\frac{1}{\Omega}\frac{d\Omega}{dc},$$

where d is a lattice constant, D_e is the thickness of the film containing vacancies, c is the concentration of defect clusters, N_d is the number of defect clusters within the film, and F is the structure factor of the unit cell. $\mathbf{q}_{||}$ and $\mathbf{Q}_{||}$ are the in-plane components while q_z and Q_z are the surface-normal components of $\mathbf{q}$ and $\mathbf{Q}$, respectively. $\mathbf{u}_{ss'}$ is the displacement vector of a Ag atom located at position s due to the defect cluster located at position s', σ is the Poisson ratio, and Ω is the volume per atom. There are several assumptions made in deriving Eq. (1) which are (i) the concentration of defects is uniform within the film, (ii) the material is elastically isotropic, and (iii) M is much smaller than unity, which corresponds to the elastic displacements being small relative to the $\mathbf{Q}$ being measured.

Although we will later show that Eq. (1) cannot be used because it employs the small-displacement approximation, this equation is nevertheless useful for understanding the impact of thin-film effects on the diffuse scattering. When $q_{||}D_e \gg 1$ in Eq. (1), only the first term in $I(\mathbf{Q})$ is significant, which reduces this result to the bulk case where the diffuse scattering intensity is proportional to $1/q^2$. Because $q_{||}D_e \gg 1$ for the

whole range of data in our experiment, we conclude that a thin-film model is unnecessary and a bulk model can be used to calculate the diffuse scattering intensity.

For a bulk material, Dederichs[18] as well as Krivoglaz[15] have calculated the diffuse intensity from defect clusters in an isotropic elastic medium where no assumption is made about the size of the displacement field and it is given by[18]

$$
\begin{aligned}
I(\mathbf{Q}) &= Ne^{-2M}|F/N_c|^2 \int \frac{d\mathbf{R}}{\Omega}\, e^{i\mathbf{q}\cdot\mathbf{R}}\,(e^{\phi(\mathbf{R})-\phi(\infty)}-1),\\
\phi(\mathbf{R}) &\equiv c\int \frac{d\mathbf{r}}{\Omega}(e^{i\mathbf{Q}\cdot(\mathbf{t}(\mathbf{r}+\mathbf{R}/2)-\mathbf{t}(\mathbf{r}-\mathbf{R}/2))}-1),\\
\phi(\infty) &\equiv -2M \equiv -2c\int \frac{d\mathbf{r}}{\Omega}(1-\cos(\mathbf{Q}\cdot\mathbf{t}(\mathbf{r}))),\\
\mathbf{t}(\mathbf{r}) &\equiv b\frac{\mathbf{r}}{r^3}, \quad \mathbf{q}\equiv \mathbf{Q}-\mathbf{Q_n},
\end{aligned}
\tag{2}
$$

where N is the number of atoms, N_c is the number of atoms per unit cell, F is the unit cell structure factor, $\mathbf{t(r)}$ is the elastic displacement at a distance r from a point defect, and b gives both the sign and strength of the point defect. By Gauss' law, this spherical defect causes a volume dilatation, $\Delta v = 4\pi b$, and, in the case of vacancies, b is negative. Note that the structure factor, which was omitted in Dederichs' paper, is included in Eq. (2). It is important that this factor is included because it contains the Q-dependent atomic form factor f_0 that varies over the large Q range of our measurements (four orders of Bragg peaks).

The static Debye-Waller factor e^{-2M} is a useful guide to the strength of the defect scattering. When M is small, Eq. (2) has the limit of the well-known $1/q^2$ dependence for the diffuse scattering intensity near a Bragg peak (Huang scattering) and $1/q^4$ in the region further away from the Bragg peak (Stokes-Wilson scattering). Note that these terms are multiplied by the static Debye-Waller factor e^{-2M} which is essentially unity for the limit of small M. M can be calculated in closed form for Eq. (2):

$$
M = c\frac{4\pi {R_c}^3}{3\Omega}\alpha, \tag{3}
$$

where $R_c = \sqrt{Q|b|}$ is the Q-dependent characteristic length scale of the problem and $\alpha = \frac{2}{5}\sqrt{2\pi} \approx 1$. Thus, the limit of the "small displacement approximation" is determined by the size of M, which depends on c, b, and Q. It can be seen in Fig. 3, however, that the diffuse scattering intensities decrease considerably with the increasing order of Bragg position K_n. This rapid decrease of intensity with K_n is also observed in Fig. 4, which shows the symmetric component of the diffuse intensity, defined as $I_{\rm sym}(q) = [I(Q_n - q) + I(Q_n + q)]/2$. Therefore, M is *not* small and the small displacement approximation is not valid for describing our data. An additional manifestation of the breakdown of the small displacement approximation can be seen in Fig. 4, where resolution-corrected $1/q^2$ and $1/q^4$ lines are plotted along with the data. All of the $1/q^2$ lines and just the $1/q^4$ line for $K_n = 2$ were placed so that they overlap with the data. The remaining $1/q^4$ lines for $K_n \neq 2$ were placed so as to intersect with the $1/q^2$ at the same q location, as suggested by Dederichs.[18] It can be seen that, with increasing K_n, the data progressively move to higher q than predicted by the $1/q^4$ lines. Moreover, in the small displacement approximation, the

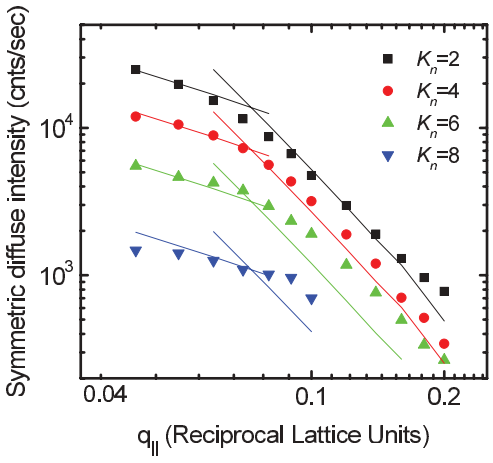

FIG. 4. (Color online) The symmetric diffuse intensity, $I_{\rm sym}(q_{||}) = [I(Q_n - q_{||}) + I(Q_n + q_{||})]/2$, is plotted for all measured orders of Bragg position K_n. Notice that the intensity decreases rapidly with increasing K_n, indicating a large static Debye-Waller factor. Also plotted are resolution-corrected $1/q^2$ and $1/q^4$ lines that show the Huang and Stokes-Wilson scattering, respectively, predicted in the small displacement approximation.

Dederichs result should be corrected so that the crossover point between the two power laws is not constant in q but, rather, it should move to *lower* $q_c \sim 1/R_c$ with increasing K_n; this will further exacerbate the disagreement of the $1/q^4$ lines with the data.

The above considerations require that Eq. (2) must be evaluated without approximation and we have done this by numerical calculation. It should be noted that there are only two variables in Eq. (2). One is b, which determines the sign and magnitude of the displacement field due to the defect clusters, and the other variable is the concentration of the defect clusters, c. The sign of b is readily determined by inspection of the data: the asymmetry observed towards the low-q side of the Bragg peak indicates vacancy clusters so that b is negative. Thus, we can determine both b and c by fitting this model to our data.

Before proceeding, two effects must be included in the model: instrumental resolution and the thermal vibration of the atomic positions. Formally, the effect of thermal vibrations can be absorbed into an effective atomic form factor,

$$
f(Q) = f_\circ(Q)\, e^{-W(Q)}, \tag{4}
$$

where $f_\circ(Q)$ is the atomic form factor for Ag. W is given by

$$
W(Q) = \frac{3h^2T}{2\pi mk\Theta^2}\left[\phi(x) + \frac{x}{4}\right]Q, \tag{5}
$$

where h is Planck's constant, k is Boltzmann's constant, and T is the absolute temperature.[20] m and Θ are the atomic mass and the Debye temperature for Ag, respectively. $x = \Theta/T$ and $\phi(x)$ is a tabulated function. For Ag, $\Theta = 210$ K so that $x = 1.4$ at $T = 150$ K, yielding $\phi(x) = 0.703$.[20] Therefore, the scattering intensity is reduced by the thermal Debye-Waller factor, $\exp(-2W)$, which is a function of K_n and it is given in Table I.

The second experimental effect concerns a correction for resolution. The diffuse scattering intensity was nominally

TABLE I. Thermal Debye-Waller factors for Ag as a function of the reciprocal-lattice unit K.

K_n	W	$\exp(-2W)$	$\exp(-2W)/0.95517$
2	0.02293	0.95517	1.0
4	0.09173	0.83239	0.87146
6	0.20639	0.66181	0.69288
8	0.36691	0.48007	0.50261

measured along K with $L = 0.1$ and the detector slit open in the surface-normal direction, which corresponds to the intensity being integrated over a small range from $L = 0.005$ to 0.15. However, the calculated diffuse scattering intensity was determined along K with $L = 0$. This is because the six-dimensional integration of Eq. (2) becomes quite complicated to evaluate, even numerically, if $\mathbf{q}$ is not parallel to $\mathbf{Q}_n$. The experimental integration and the calculation direction are schematically shown in Fig. 1. Because the effect of integration is relatively insensitive to the precise form of the diffuse scattering, we estimated the effect of integration using Eq. (1) ($= 1/q^2$ in the thick-film limit), which is much easier to evaluate than the numerical evaluation of Eq. (2). Figure 5 shows a comparison of the integrated and nonintegrated diffuse intensity calculated in this manner at $K_n = 2$. It can be seen that the effect of integration is to reduce the diffuse intensity near the Bragg peak; the results are independent of K_n. Note that there are no asymmetric distortions of the diffuse intensity due to the effect of resolution. Therefore, a resolution correction factor, defined as the ratio of the integrated to the nonintegrated diffuse intensity, was applied to the diffuse intensity calculated from Eq. (2) for the purpose of comparing to the experimentally measured diffuse intensity.

Figure 6 compares the experimental data and the numerical calculation of diffuse scattering intensity. The model of Eq. (2) contains two parameters for the vacancy clusters, the strength of their displacement field b, and their concentration c. The best agreement between the model and data occurs for $b = -60 \pm 15$ (Å^3) and $c = 0.0005 \pm 0.0002$. To demonstrate the sensitivity to the model parameters, two other curves are also

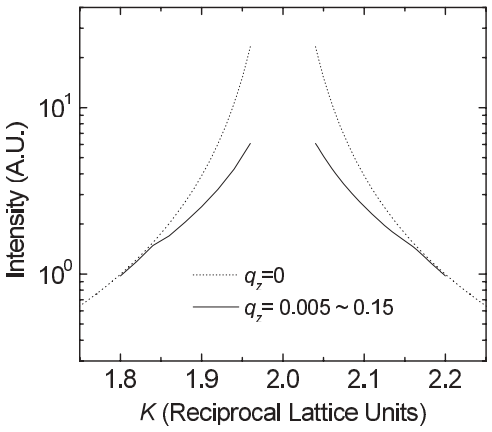

FIG. 5. The effect of resolution is shown by comparing the diffuse intensity calculated for $q_z = 0$ (dotted line) with the same intensity integrated over the experimental resolution, $q_z = 0.005 \sim 0.15$ (solid line).

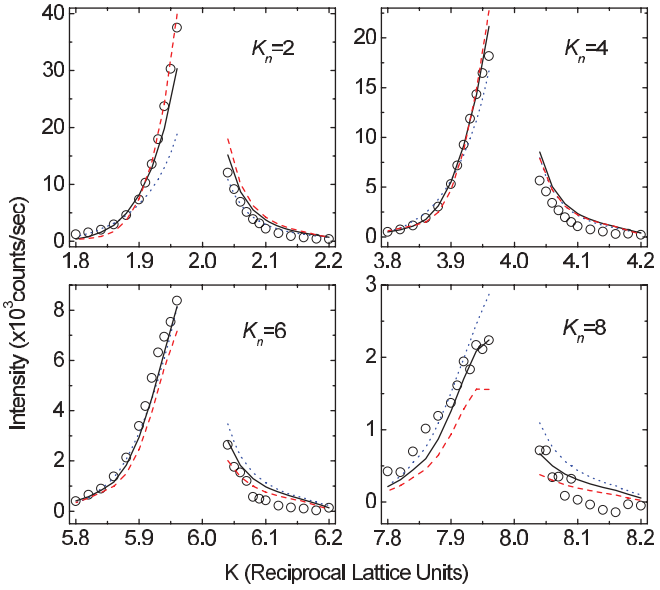

FIG. 6. (Color online) Comparison of the measured diffuse scattering intensity (circles) and the numerically calculated intensities (lines). Dotted (blue), solid (black), and dashed (red) lines are for $-b = 30$, 60, and 100, respectively.

presented in Fig. 6 for comparison. In the plots, the product bc was held fixed to the best-fit value because the model is extremely sensitive to this product and the curves would be very far from the data if this were not done. Using the best-fit parameters, the model compares well with the experimental data over the entire data range. Moreover, it can be seen that having data for four orders of Bragg positions provides a discerning measure of the model parameters.

A comparison of the model and experimental data can also be examined in a different way by plotting the symmetric intensity and the antisymmetric intensity, defined as $I_{\mathrm{sym}}(q_{||}) = [I(Q_n - q_{||}) + I(Q_n + q_{||})]/2$ and $I_{\mathrm{anti-sym}}(q_{||}) = [I(Q_n - q_{||}) - I(Q_n + q_{||})]/2$, respectively, as shown in Fig. 7. From these plots, which are shown on a logarithmic intensity scale, it can be seen that the model does a good job of capturing the strong variation of intensity *between* different orders of Bragg positions. Moreover, as can be seen in Fig. 7(a), *within* a given Bragg position the large change in symmetric intensity with $q_{||}$ is well described by the model, including the curvature of the data. This is in stark contrast to any attempt to use simple $1/q_{||}^2$ and $1/q_{||}^4$ power laws, as discussed in connection with Fig. 4. Therefore, these plots clearly illustrate the necessity to use the complete diffuse scattering formalism of Eq. (2). Although the overall intensity variation between Bragg positions for the antisymmetric intensity in Fig. 7(b) is well described by the model, the quality of fit is not nearly as good as for the symmetric part. Above $q_{||} > 0.1$ the agreement is quite poor. It should be noted, however, that the antisymmetric intensity involves taking the *difference* of intensity and it is, therefore, quite sensitive to other effects that have not been considered. Experimentally, the difference intensity can be affected by small systematic errors that are difficult to estimate, particularly at large $q_{||}$ where the intensity is very low. Similarly, the model makes a number of assumptions that will ultimately break down at some point. For example, the

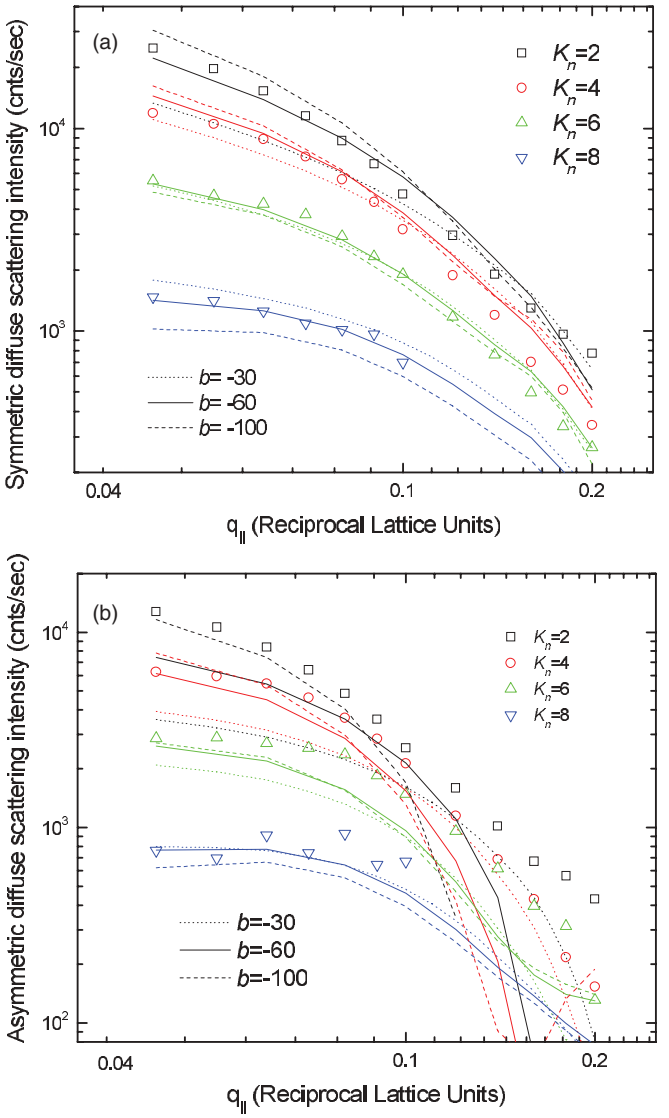

FIG. 7. (Color online) The symmetric and antisymmetric components of the experimental diffuse intensities are shown on a logarithmic scale for the four measured Bragg positions, along with the same calculated curves as shown in Fig. 6.

vacancy clusters are assumed to be spherical when, in fact, there could be uniaxial anisotropic effects due to the thin-film geometry. Cubic crystalline anisotropy was not included and there is likely to be a distribution of cluster sizes, which also was not accounted for. We expect that these effects would only give small quantitative changes within the given error bars, rather than qualitatively change the results. Finally, an elastic continuum theory is used and, for larger $q_{||}$, atomistic effects are certainly expected to become important. Nevertheless, we have demonstrated that the spherical cluster model which numerically integrates Eq. (2) agrees reasonably well with the experimental measurements on a logarithmic intensity scale.

It is useful to emphasize that the K_n dependence of the diffuse scattering is extremely sensitive to the size of the dilatation due to the vacancy clusters, as illustrated in Fig. 8. For a small dilatation ($b = -1$, which would roughly correspond to a monovacancy, as discussed below) the diffuse

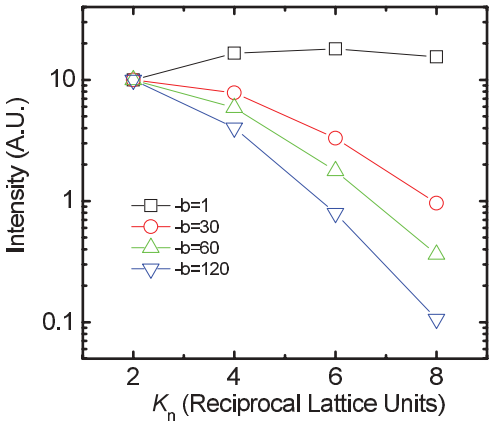

FIG. 8. (Color online) Calculated diffuse scattering intensity at $q = 0.02$ as a function of K_n for different defect cluster sizes. For a monovacancy, the intensity initially increases with K_n, but for larger clusters the diffuse intensity decreases monotonically. The lines are a guide for the eye.

scattering intensity initially *increases* as a function of K_n, whereas the diffuse intensity monotonically *decreases* for much larger values of b. Moreover, the diffuse intensity decreases more rapidly with K_n as the dilatation b increases. Therefore, from the experimentally measured diffuse intensity in Fig. 3, one can qualitatively determine that the vacancy clusters are quite large. Additionally, the detailed shape of the $\mathbf{q}_{||}$ dependence of the diffuse scattering intensity depends strongly on K_n and this imposes useful constraints on the model of Eq. (2) which, for large clusters, differs significantly from Huang and Stokes-Wilson scattering. Therefore, it can be seen that measuring the diffuse scattering for a range of Bragg positions places stringent constraints on the determination of the size of the dilatation caused by the clusters.

The vacancy cluster size can be roughly estimated from the strength of the displacement field b which was determined in our experiments. Given that the local elastic volume dilatation[21] around a defect is given by $\Delta v = 4\pi b$, then using our best-fit value of $b = -60$ yields $\Delta v = -750$ Å^3, which corresponds to ~45 atomic volumes. However, this is an elastic dilatation volume and not the volume of the missing atoms in a cluster. To crudely estimate the latter, we refer to studies of monovacancies in noble metals which show that the elastic dilatation volume is less than half of the atomic volume of the vacancy.[22,23] This would suggest that there are on the order of 100 missing atoms in a vacancy cluster. Independent of the precise number in a cluster, however, it is clear that the system contains a low concentration of very large vacancy clusters.

The *local* dilatation around a defect is elastically related to the *macroscopic* homogeneous strain that is measured by diffraction (or reflectivity). In the latter case, the homogeneous relative volume change is given by[21]

$$\frac{\Delta V}{V} = 3\frac{1-\sigma}{1+\sigma}\frac{\Delta v}{\Omega}c, \tag{6}$$

where σ is Poisson's ratio for the metal. Using $\sigma = 0.37$ for Ag and the best-fit values of b and c, we obtain a relative lattice constant change $\frac{\Delta d}{d} = \frac{1}{3}\frac{\Delta V}{V} = -0.01$ that corresponds well to prior x-ray reflectivity measurements.[5] Therefore,

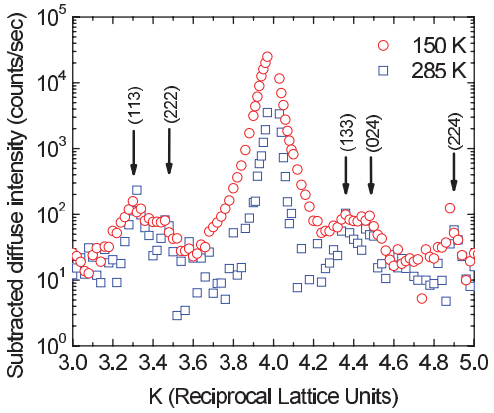

FIG. 9. (Color online) Diffuse scattering intensity as a function of K at $L = 0.02$ for two different growth temperatures: 285 K (squares) and 150 K (circles).

both length scales measured by x-ray scattering—the local dilatation and the homogenous strain—are in good agreement with one another.

In addition to the diffuse scattering due to vacancies that appears around the Bragg peaks, several small peaks far away from the single-crystal Bragg peaks were also observed after deposition. Figure 9 shows measurements from two films grown at different temperatures. It can be seen that, besides the Bragg peak at $K = 4$ and the diffuse scattering around it, both films exhibit small peaks at $K = 3.3$, 3.45, 4.33, 4.45, and 4.87. These positions correspond to the bulk Ag reflections of (113), (222), (133), (024), and (224), which suggests the presence of randomly oriented bulk crystallites of Ag. Indeed, a two-dimensional map of the scattering around the $K = 4$ Bragg position in Fig. 10 clearly shows the circular distribution of scattering intensity, which confirms the powder diffraction. These powder peaks are not observed on the starting Ag single-crystal substrate and, therefore, the randomly oriented

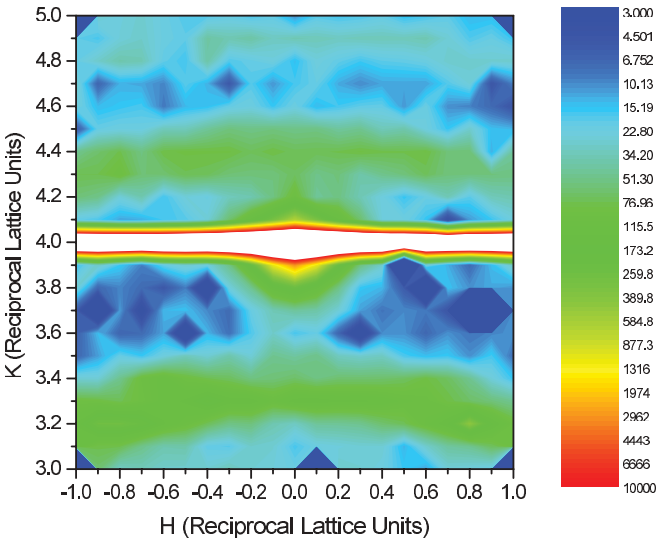

FIG. 10. (Color online) Contour map of the diffuse scattering intensity near the (0, 4, 0) Bragg peak which shows the arc-shaped intensity distribution of powder peaks. The white strip at the center of the map is an artifact because no data were taken there.

crystallites form as a result of the deposition. Tiny crystallites were observed by visual inspection of the sample after it was removed from the vacuum system, indicating that the crystallites are macroscopic in size. These results indicate that nonepitaxial crystallites form by random nucleation and continue to grow during the deposition of 100 MLs.

It is important to note that the crystallites do not influence the diffuse scattering intensity observed around the Bragg reflections of the single-crystal substrate. As seen in Fig. 9, at the higher growth temperature the diffuse scattering decreases by approximately a factor of 10, whereas the powder peaks of the crystallites do not change with temperature. Therefore, the formation of the crystallites occur independently of the vacancy cluster mechanism in the *homoepitaxial* film that grows on the single-crystal substrate.

Although a detailed temperature dependence was not studied, Fig. 9 shows that the diffuse scattering from the vacancy clusters does not completely disappear at the higher measured temperature of 285 K. By assuming the same cluster size as for the film grown at 150 K, the concentration of vacancy clusters in the film grown at 285 K is estimated to be almost 30 times smaller than that of the 150-K film. The measurable amount of diffuse scattering from the film grown at 285 K demonstrates that diffuse scattering measurements are quite sensitive to a very small concentration of vacancy clusters. It is significantly more sensitive than the x-ray reflectivity experiments.[5]

Finally, we consider the effect of the missing atoms on the diffuse scattering. The model of Eq. (2) includes only the displacement of the atoms by the vacancy clusters and it neglects the effect of the missing atoms in the cluster. Although this is a commonly used approximation because it is known that the phase is more important than the amplitude, particularly at large K_n, we can estimate the magnitude of the neglected volume scattering from the nanocavities themselves. If we assume that the nanocavities are randomly distributed in the film in such a way that their scattering amplitudes do not interfere, we can use Babinet's principle which states that the missing intensity distribution due to the cavities is the same as that from a set of crystals with the same sizes, shapes, and orientations as those of the cavities. To make the calculation simpler, we calculate the scattering intensity from a nanocrystal of Ag with the dimension of $2 \times 3 \times 3$ unit cells, which contains 72 Ag atoms. The intensity of this small crystal is given by

$$\begin{aligned} I(\mathbf{Q})_{\mathrm{cav}} &= N_{\mathrm{cav}} |F|^2 \left| \sum_s e^{iQr_s} \right|^2 \\ &= N_{\mathrm{cav}} |F|^2 \left| \sum_{n_x=0}^{1} \sum_{n_y=0}^{2} \sum_{n_z=0}^{2} e^{2\pi i (K n_y)} \right|^2 \\ &= 36 N_{\mathrm{cav}} |F|^2 |1 + e^{i2\pi K} + e^{i4\pi K}|^2, \end{aligned} \tag{7}$$

where N_{cav} is the number of cavities within the film, F is a structure factor of Ag unit cell, $\mathbf{Q} = (0, K, 0)$. If we compare $I(\mathbf{Q})_{\mathrm{cav}}$ with $I(\mathbf{Q})$ from Eq. (2), we find that the volume scattering intensity from the nanocavities is five orders of magnitude weaker than the diffuse scattering intensity from the displaced atoms surrounding the cavities, thereby justifying the neglect of the volume contribution in Eq. (2).

IV. CONCLUSIONS

In conclusion, the x-ray diffuse scattering measurements reported here are accurately described by a point-defect scattering model where there is excellent agreement between the model calculations and the data over a broad range in q as well as over four different orders of Bragg positions K_n. These results indicate that large vacancy clusters are incorporated into 100-ML Ag(001) films which are grown homoepitaxially at low temperature. The long-range strain computed from our diffuse scattering experiments also agrees well with previous x-ray reflectivity measurements.[5] Because of the strong displacement field associated with the large size of the vacancy clusters, we have demonstrated that the conventional Huang and Stokes-Wilson scattering regimes cannot be assumed and that one must numerically integrate the full diffuse scattering model.

Although these experiments are well described by a point-defect distortion caused by large vacancy clusters, there remain interesting and important questions about how nanoscale asperities at the surface lead to elastic distortions. Simulation studies of relatively thin films deposited at grazing angles suggest the development of nanoscale roughness that leads to surface strains.[10] However, a connection between those simulations and the present work is difficult to make because our films were quite thick (100 MLs) and they were deposited at near-normal (30°). Future experiments on thinner films and performed as a function of deposition angle are required in order to explore the effect of nanoscale surface roughness effects.

ACKNOWLEDGMENTS

Support is gratefully acknowledged from the National Science Foundation, Grant No. DMR0706278. The Advanced Photon Source is supported by DOE Office of Basic Energy Sciences under Contract No. W-31-109-Eng-38, and the Sector 6 beam line received support through the Ames Laboratory under Contract No. DOE W-7405-Eng-82. C.K. was supported by MEST and PAL, XFEL project, Korea.

*micelip@missouri.edu

[1] J. W. Evans, P. A. Thiel, and M. C. Bartelt, Surf. Sci. Rep. **61**, 1 (2006).
[2] J. W. Evans, D. E. Sanders, P. A. Thiel, and A. E. DePristo, Phys. Rev. B **41**, 5410 (1990).
[3] J. G. Amar and F. Family, Phys. Rev. B **54**, 14742 (1996).
[4] C. E. Botez, W. C. Elliott, P. F. Miceli, and P. W. Stephens, Phys. Rev. B **66**, 075418 (2002).
[5] C. E. Botez, K. Li, E. D. Lu, W. C. Elliott, P. F. Miceli, E. H. Conrad, and P. W. Stephens, Appl. Phys. Lett. **81**, 4718 (2002).
[6] C. E. Botez, P. F. Miceli, and P. W. Stephens, Phys. Rev. B **66**, 195413 (2002).
[7] C. R. Stoldt, K. J. Caspersen, M. C. Bartelt, C. J. Jenks, J. W. Evans, and P. A. Thiel, Phys. Rev. Lett. **85**, 800 (2000).
[8] K. J. Caspersen, C. R. Stoldt, A. R. Layson, M. C. Bartelt, P. A. Thiel, and J. W. Evans, Phys. Rev. B **63**, 085401 (2001).
[9] K. J. Caspersen and J. W. Evans, Phys. Rev. B **64**, 075401 (2001).
[10] Y. Shim, V. Borovikov, B. P. Uberuaga, A. F. Voter, and J. G. Amar, Phys. Rev. Lett. **101**, 116101 (2008).
[11] C. Kim, R. Feng, E. H. Conrad, and P. F. Miceli, Appl. Phys. Lett. **91**, 093131 (2007).
[12] A. Kara and T. S. Rahman, Phys. Rev. Lett. **81**, 1453 (1998).
[13] B. Barnes, U. Bangert, and P. Martineau, Phys. Status Solidi A **203**, 3081 (2006).
[14] I. Mukouda, Y. Shimomura, and M. Kiritani, Mater. Sci. Eng. A **350**, 37 (2003).
[15] M. A. Krivoglaz, *X-ray and Neutron Diffraction in Nonideal Crystal* (Springer, New York, 1996).
[16] P. H. Dederichs, J. Phys. F **3**, 471 (1973).
[17] P. Ehrhart, J. Nucl. Mater. **69**, 200 (1978).
[18] P. H. Dederichs, Phys. Rev. B **4**, 1041 (1971).
[19] R. I. Barabash and M. A. Krivoglaz, Sov. Phys. Solid State **29**, 1768 (1987).
[20] B. D. Cullity, *Elements of X-ray Diffraction* (Addison-Wesley, Reading, MA, 1978).
[21] J. D. Eshelby, J. Appl. Phys. **25**, 255 (1954).
[22] C. W. Tucker and J. B. Sampson, Acta Metall. **2**, 433 (1954).
[23] P. Ehrhart, K. H. Robrock, and H. R. Shober, *Physics of Radiation Effects in Crystals* (Elsevier, New York, 1986).